

# Graph-Guided Fused Regularization for Single- and Multi-Task Regression on Spatiotemporal Data

Meixia Lin\*

Ziyang Zeng†

Yangjing Zhang‡

February 17, 2026

## Abstract

Spatiotemporal matrix-valued data arise frequently in modern applications, yet performing effective regression analysis remains challenging due to complex, dimension-specific dependencies. In this work, we propose a regularized framework for spatiotemporal matrix regression that characterizes temporal and spatial dependencies through tailored penalties. Specifically, the model incorporates a fused penalty to capture smooth temporal evolution and a graph-guided penalty to promote spatial similarity. The framework also extends to the multi-task setting, enabling joint estimation across related tasks. We provide a comprehensive analysis of the framework from both theoretical and computational perspectives. Theoretically, we establish the statistical consistency of the proposed estimators. Computationally, we develop an efficient solver based on the Halpern Peaceman-Rachford method for the resulting composite convex optimization problem. The proposed algorithm achieves a fast global non-ergodic  $\mathcal{O}(1/k)$  convergence rate with low per-iteration complexity. Extensive numerical experiments demonstrate that our method significantly outperforms state-of-the-art approaches in terms of predictive accuracy and estimation error, while also exhibiting superior computational efficiency and scalability.

## 1 Introduction

We consider the matrix regression model

$$y_k = \langle X_k, \theta \rangle + \varepsilon_k, \quad k \in [n] := \{1, \dots, n\}, \quad (1)$$

where  $n$  is the sample size,  $y_k \in \mathbb{R}$  is the scalar response, and  $\varepsilon_k$  denotes the observation noise. The unknown regression coefficient  $\theta \in \mathbb{R}^{t \times s}$  and the predictors  $X_k \in \mathbb{R}^{t \times s}$  are matrices that encode spatiotemporal structures, with rows and columns representing  $t$  time lags and  $s$  spatial locations, respectively, as commonly encountered in applications such as climate modeling (e.g., sea surface temperature data).

One line of existing approaches relies on sparsity-inducing penalties like the lasso [1], structured sparsity regularizations including the fused lasso [2] and group lasso [3], as well as low-rank regularization [4]. However, these methods may fail to fully exploit the intrinsic spatiotemporal dependencies in the predictors. To address this, another line of work assumes that the regression coefficient aligns well with the correlation structure of the predictors, and employs graph total variation (GTV) regularization to promote similarity among highly correlated variables (see, e.g., [5–8]). These approaches typically treat time lags and spatial locations jointly and

\*Engineering Systems and Design, Singapore University of Technology and Design, Singapore (e-mail: meixia.lin@sutd.edu.sg).

†Department of Industrial Systems Engineering and Management, National University of Singapore (e-mail: ziyangzeng@u.nus.edu).

‡The State Key Laboratory of Mathematical Sciences, Academy of Mathematics and Systems Science, Chinese Academy of Sciences, Beijing, China (e-mail: yangjing.zhang@amss.ac.cn).

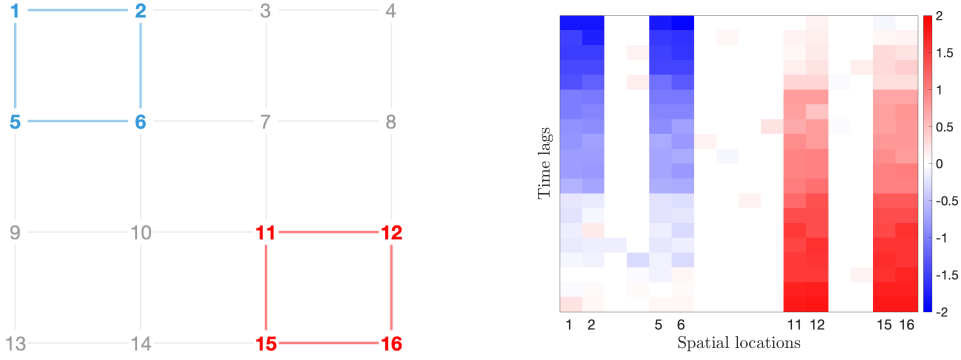


Figure 1: Illustrative spatiotemporal structure in the coefficient matrix. Left: Spatial graph on a  $4 \times 4$  grid, where blue and red groups highlight sets of adjacent locations. Right: Estimated coefficient matrix  $\theta$ , exhibiting smooth evolution over time lags, and similarity among adjacent spatial locations.

rely heavily on estimating a  $ts \times ts$  covariance (cf. (4)). In practice, an accurate estimation of such a covariance can be statistically challenging and often requires substantial side information. Moreover, such joint modeling may overlook dimension-specific characteristics inherent in spatiotemporal data, where temporal evolution is smooth and adjacent locations exhibit similar behavior (see Fig. 1).

Motivated by these considerations, we propose a regularized framework that treats time lags and spatial locations separately, encouraging smooth temporal evolution and local spatial similarity. Specifically, we impose a fused penalty along the temporal dimension to promote smoothness across time lags, and a graph-guided regularization across spatial locations to encourage similar behaviors among adjacent regions. Unlike existing GTV-based approaches that rely on estimating a  $ts \times ts$  covariance matrix, our method only uses a prespecified  $s \times s$  spatial graph, constructed directly from geographic proximity or simply a lattice structure when side information is unavailable.

We further consider a multi-task extension

$$y_k^{(r)} = \langle X_k, \theta^{(r)} \rangle + \varepsilon_k^{(r)}, \quad k \in [n], r \in [m], \quad (2)$$

where each task  $r$  has its own regression coefficient  $\theta^{(r)} \in \mathbb{R}^{t \times s}$ , response  $y_k^{(r)} \in \mathbb{R}$  and noise  $\varepsilon_k^{(r)}$ , while the predictors  $X_k \in \mathbb{R}^{t \times s}$  are shared across tasks. To capture relationships among tasks, we adopt a common multi-task learning strategy based on joint  $\ell_2$ -type regularization, which encourages similar support patterns and information sharing across tasks; see, e.g., [6, (3)], [9, (3)].

Altogether, we integrate the aforementioned components into a unified framework for single- and multi-task spatiotemporal regression, which is formulated as a composite convex optimization problem that combines a sparsity-inducing  $\ell_1$  penalty, a fused temporal penalty, a graph-guided spatial penalty, and, in the multi-task setting, an additional  $\ell_2$  penalty. A standard method for such problems is the alternating direction method of multipliers (ADMM) [10–12]. However, ADMM is known to achieve only non-ergodic rates of  $o(1/\sqrt{k})$  for primal feasibility and objective gap [13], and  $\mathcal{O}(1/\sqrt{k})$  for Karush-Kuhn-Tucker (KKT) residual [14], motivating the development of accelerated variants. A recent and effective acceleration strategy incorporates the Halpern's iteration into classical operator splitting schemes. In particular, Zhang et al. [15] proposed the Halpern Peaceman–Rachford (HPR) method and established a non-ergodic  $\mathcal{O}(1/k)$  convergence rate for both the KKT residual and the primal objective gap. Subsequent work showed that HPR is equivalent to a Halpern-accelerated ADMM [16], and similar acceleration guarantees were obtained for proximal ADMM schemes [17]. Beyond theoretical improvements, HPR has shown strong practical performance in linear programming [16], con-

vex quadratic programming [18], and optimal transport [19]. These developments motivate the adoption of an HPR-based algorithm for efficiently computing our proposed estimator.

Our main contributions are summarized as follows.

- We propose a unified regularized framework for single- and multi-task spatiotemporal matrix regression that separately models temporal smoothness and spatial similarities, and we further establish the consistency of the proposed estimator.
- Unlike existing GTV-based approaches [5–8], the proposed method avoids estimating high-dimensional  $ts \times ts$  covariance matrices and only uses a prespecified  $s \times s$  spatial graph, which can be constructed directly from geographic proximity or a simple lattice structure.
- We develop an efficient HPR-based algorithm for the resulting composite convex optimization problem with provable non-ergodic  $\mathcal{O}(1/k)$  convergence guarantees, and demonstrate its practical advantages through extensive numerical experiments.

The rest of the paper is organized as follows. Section 2 introduces the proposed single- and multi-task estimators. Section 3 establishes their consistency properties. Section 4 develops an efficient HPR-based algorithm for solving the resulting regularized matrix regression problems. Extensive numerical experiments are presented in Section 5, and we conclude in Section 6.

**Notations.** Let  $[n] := \{1, \dots, n\}$  and  $I_s$  be the  $s \times s$  identity matrix (or simply  $I$  when the dimension is clear from the context). The symbol  $\otimes$  denotes the Kronecker product. For a matrix  $A$ ,  $\text{sgn}(A)$  is applied componentwise, where for  $t \in \mathbb{R}$ ,  $\text{sgn}(t) = 1$  if  $t > 0$ ,  $\text{sgn}(t) = 0$  if  $t = 0$ , and  $\text{sgn}(t) = -1$  if  $t < 0$ . For a set  $C$ , the characteristic function  $\mathbb{I}_C$  is defined as  $\mathbb{I}_C(x) = 1$  if  $x \in C$  and  $\mathbb{I}_C(x) = 0$  otherwise. For a vector  $x$ ,  $\|x\|_q$  denotes its  $\ell_q$  norm. For a matrix  $X$ ,  $X_{i \cdot}$  and  $X_{\cdot j}$  denote its  $i$ -th row and  $j$ -th column, respectively. For a collection of matrices  $\{A^{(r)}\}_{r=1}^m$ , we define its Frobenius norm as  $\|\{A^{(r)}\}_{r=1}^m\|_F := (\sum_{r=1}^m \|A^{(r)}\|_F^2)^{1/2}$ . Let  $h : \mathbb{R}^n \rightarrow (-\infty, \infty]$  be a closed proper convex function, the proximal mapping of  $h$  at  $x$  is defined as  $\text{prox}_h(x) := \arg \min_{y \in \mathbb{R}^n} \{h(y) + \frac{1}{2}\|y - x\|^2\}$ .

## 2 Model Formulation

In this section, we formally present our regression frameworks for both single- and multi-task settings. Building upon the motivations in Section 1, we design estimators that simultaneously capture sparsity, temporal smoothness, and spatial similarities. We first formalize the single-task model in Section 2.1, then extend it to the multi-task setting in Section 2.2, where the coefficient matrices of related tasks are estimated jointly to promote information and sparsity sharing.

### 2.1 GGFL: Single-Task Model

Given observations  $\{(X_k, y_k) \mid k \in [n]\}$  from model (1), we define the linear operator  $\mathcal{X} : \mathbb{R}^{t \times s} \rightarrow \mathbb{R}^n$  by  $\mathcal{X}(\theta) = [\langle X_1, \theta \rangle, \dots, \langle X_n, \theta \rangle]^\top$ ,  $\theta \in \mathbb{R}^{t \times s}$ , and the response vector  $y = [y_1, \dots, y_n]^\top \in \mathbb{R}^n$ . We propose the *graph-guided (group) fused lasso (GGFL)* model:

$$\min_{\theta \in \mathbb{R}^{t \times s}} \left\{ f(\theta; \mathcal{X}, y) := \frac{1}{2} \|y - \mathcal{X}(\theta)\|_2^2 + \lambda_1 \|\theta\|_1 + \lambda_t \sum_{i=1}^{t-1} \|\Delta_t^i \theta\|_p + \lambda_g \sum_{(j, j') \in \mathcal{E}} w_{jj'} \|\Delta_g^{jj'} \theta\|_q \right\}, \quad (3)$$

where  $\Delta_t^i \theta := \theta_{i \cdot} - \theta_{(i+1)\cdot} \in \mathbb{R}^s$ ,  $\Delta_g^{jj'} \theta := \theta_{\cdot j} - \theta_{\cdot j'} \in \mathbb{R}^t$ . Here,  $\mathcal{E}$  and  $w_{jj'}$  represent the edge set and corresponding weights of a prespecified spatial graph,  $\lambda_1, \lambda_t, \lambda_g > 0$  are regularization parameters, and  $p, q \geq 1$  specify the norms.

The regularization terms enforce specific structural assumptions. First, the  $\ell_1$ -penalty ( $\lambda_1$ ) induces entry-wise sparsity. Second, the fused temporal penalty ( $\lambda_t$ ) promotes similarities between adjacent time steps, inducing a smooth evolution over time. Third, the graph-guided spatial penalty ( $\lambda_g$ ) encodes structure via the weighted graph  $\mathcal{G} = \{[s], \mathcal{E}, (w_{jj'})\}$ , where the weights  $w_{jj'}$  (e.g., inverse distance) quantify pairwise similarity to enforce local consistency among geographically adjacent or related locations.

The choice of norms  $p$  and  $q$  determines the structure of the penalized differences. Setting  $p = q = 1$  enforces coordinate-wise sparsity, while choosing  $p, q > 1$  (e.g.,  $p = q = 2$  in our experiments) induces group-level sparsity, encouraging the entire difference vector to be zero [20].

**Remark 1** (Relation to the graph total variation (GTV) estimator). *The case of  $p = q = 1$  in (3) is conceptually related to the GTV estimator [8, (4)], which minimizes*

$$\min_{\theta \in \mathbb{R}^{t \times s}} \left\{ \frac{1}{n} \|y - \mathcal{X}(\theta)\|_2^2 + \lambda_1 \|\theta\|_1 + \lambda_{tv} \sum_{(ij), (i'j')} |\Sigma_{(ij), (i'j')}|^{\frac{1}{2}} |\theta_{ij} - s_{(ij), (i'j')} \theta_{i'j'}| \right\}, \quad (4)$$

where  $\Sigma \in \mathbb{S}_+^{ts}$  is the covariance matrix of the vectorized predictors  $[\text{vec}(X_1), \dots, \text{vec}(X_n)]^\top$  estimated in a prior step, with  $s := \text{sgn}(\Sigma)$ . The last penalty term in (4) represents the total variation of the signal  $\theta$  over a graph defined by  $\Sigma$ . While the GTV estimator promotes similarity among predictors via the weighted differences  $|\theta_{ij} - s_{(ij), (i'j')} \theta_{i'j'}|$ , it treats temporal and spatial dependencies uniformly via a single large covariance matrix  $\Sigma$ . In contrast, our model (3) separates the spatial and temporal structures via distinct fused and graph-guided penalties, thereby avoiding the estimation of a large covariance matrix.

In fact, (4) aligns with our model (3) under specific structural assumptions. Suppose the covariance admits a Kronecker sum form  $\Sigma = \Sigma_s \oplus \Sigma_t := \Sigma_s \otimes I_t + I_s \otimes \Sigma_t$ , where  $\Sigma_t \in \mathbb{S}_+^t$  and  $\Sigma_s \in \mathbb{S}_+^s$  represent temporal and spatial covariance matrices, respectively. The GTV penalty (last term in (4)) decouples into additive temporal and spatial components:

$$\lambda_{tv} \sum_{i, i'} |(\Sigma_t)_{ii'}|^{\frac{1}{2}} \|\theta_{i \cdot} - \text{sgn}((\Sigma_t)_{ii'}) \theta_{i' \cdot}\|_1 + \lambda_{tv} \sum_{j, j'} |(\Sigma_s)_{jj'}|^{\frac{1}{2}} \|\theta_{\cdot j} - \text{sgn}((\Sigma_s)_{jj'}) \theta_{\cdot j'}\|_1.$$

Specifically, if we assume

$$(\Sigma_t)_{ii'} = \begin{cases} (\lambda_t/2)^2, & |i - i'| = 1, \\ 0, & |i - i'| > 1, \end{cases} \quad (\Sigma_s)_{jj'} = \begin{cases} (\lambda_g w_{jj'})^2, & (j, j') \in \mathcal{E}, \\ 0, & (j, j') \notin \mathcal{E} \text{ and } j' \neq j, \end{cases}$$

the GTV formulation (4) is equivalent to our model (3) with  $p = q = 1$  by ignoring the constant scaling of the loss.

## 2.2 MultiGGFL: Multi-Task Model

Given observations  $\{(X_k, y_k^{(r)}) \mid k \in [n], r \in [m]\}$  from model (2), we define the response vector of task  $r$  by  $y^{(r)} = [y_1^{(r)}, \dots, y_n^{(r)}]^\top \in \mathbb{R}^n$ , and collect the regression coefficient  $\theta^{(r)}$  into a third-order tensor  $\Theta \in \mathbb{R}^{t \times s \times m}$  with the  $r$ -th slice  $\Theta^{(r)} = \theta^{(r)}$ . Let  $\Theta_{ij}^{(r)}$  denote the  $(i, j)$ -th entry of  $\Theta^{(r)}$ , and define  $\Theta_{[ij]} := [\Theta_{ij}^{(1)}, \Theta_{ij}^{(2)}, \dots, \Theta_{ij}^{(m)}]^\top \in \mathbb{R}^m$ . See Fig. 2 for an illustration of these notations. Based on this setup, we propose the *multi-task graph-guided (group) fused lasso (MultiGGFL)* model:

$$\min_{\Theta \in \mathbb{R}^{t \times s \times m}} \sum_{r=1}^m f(\Theta^{(r)}; \mathcal{X}, y^{(r)}) + \lambda_2 \sum_{i=1}^t \sum_{j=1}^s \|\Theta_{[ij]}\|_2. \quad (5)$$

Here  $f(\Theta^{(r)}; \mathcal{X}, y^{(r)})$  denotes the single-task GGFL objective (3) for task  $r$ , and the second term with parameter  $\lambda_2 \geq 0$  promotes shared sparsity patterns across tasks by encouraging the grouped coefficients  $\Theta_{[ij]}$  to be zero vectors. This group-wise penalty term is widely used in the learning of multiple tasks, see, e.g., [6, (3)], [9, (3)]. When  $\lambda_2 = 0$ , this model decouples into  $m$  independent single-task GGFL problems; furthermore, if  $m = 1$ , it reduces to the single-task GGFL (3).

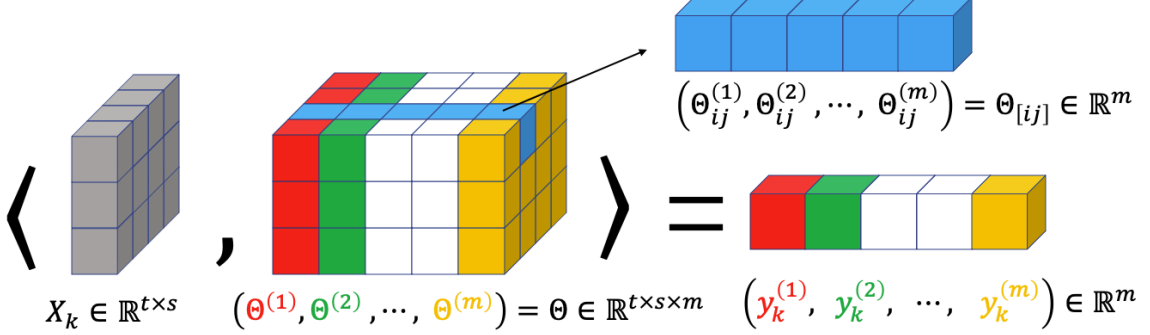


Figure 2: Illustration of multi-task model (2) and its notations. Each cube represents a coefficient. The highlighted blue cuboid corresponds to the grouped coefficient vector  $\Theta_{[ij]}$  across tasks.

### 3 Consistency Analysis

In this section, we establish consistency analysis for the multi-task estimator (5), from which the single-task case follows as a special case.

To this end, we begin by stating a set of regularity assumptions that are standard in the consistency analysis of statistical estimators [21–23]. Let  $\varepsilon_k = [\varepsilon_k^{(1)}, \varepsilon_k^{(2)}, \dots, \varepsilon_k^{(m)}]^\top \in \mathbb{R}^m$  denote the vector of noise terms for the  $k$ -th observation, and let  $\varepsilon^{(r)} = [\varepsilon_1^{(r)}, \varepsilon_2^{(r)}, \dots, \varepsilon_n^{(r)}]^\top \in \mathbb{R}^n$  denote the noise vector for task  $r$ .

**Assumption 1.** *The sequence  $\{\varepsilon_k \mid k \in [n]\}$  consists of independent and identically distributed random vectors satisfying  $\mathbb{E}[\varepsilon_k] = 0$  and  $\mathbb{E}[\varepsilon_k \varepsilon_k^\top] = \Sigma_\varepsilon$ .*

**Assumption 2.** *The empirical covariance operator of the predictors converges to a positive definite limit, i.e.,*

$$\mathcal{M}_n := \frac{1}{n} \mathcal{X}^* \mathcal{X} \longrightarrow \mathcal{M},$$

for some self-adjoint positive definite operator  $\mathcal{M} : \mathbb{R}^{t \times s} \rightarrow \mathbb{R}^{t \times s}$ .

Under Assumptions 1 and 2, there exists a tensor  $\Xi \in \mathbb{R}^{t \times s \times m}$  whose slices  $\Xi^{(r)}$ 's are mean-zero Gaussian matrices in  $\mathbb{R}^{t \times s}$  satisfying

$$\text{Cov}((\Xi^{(r)})_{ij}, (\Xi^{(r')})_{i'j'}) = (\Sigma_\varepsilon)_{rr'} \langle E_{ij}, \mathcal{M}(E_{i'j'}) \rangle, \quad (6)$$

for all  $r, r' \in [m]$ ,  $i, i' \in [t]$ ,  $j, j' \in [s]$ , such that, for each  $r \in [m]$ ,

$$\Xi_n^{(r)} = \frac{1}{\sqrt{n}} \mathcal{X}^* \varepsilon^{(r)} \rightarrow \Xi^{(r)}$$

in distribution as  $n \rightarrow \infty$ . Here  $E_{ij} \in \mathbb{R}^{t \times s}$  denote the matrix with a one in position  $(i, j)$  and zeros elsewhere.

Moreover, Assumption 2 ensures that, for sufficiently large  $n$ , the operator  $\mathcal{X}^* \mathcal{X}$  is nonsingular, which guarantees the existence of a unique minimizer of the empirical objective in (5). We therefore focus on the following equivalent formulation of the MultiGGFL model (5):

$$\begin{aligned}\widehat{\Theta}_n = & \arg \min_{\Upsilon \in \mathbb{R}^{t \times s \times m}} \sum_{r=1}^m \frac{1}{2} \|y^{(r)} - \mathcal{X}(\Upsilon^{(r)})\|_2^2 \\ & + \lambda_{t,n} \sum_{r=1}^m \sum_{i=1}^{t-1} \|\Delta_t^i \Upsilon^{(r)}\|_p + \lambda_{g,n} \sum_{r=1}^m \sum_{(j,j') \in \mathcal{E}} w_{jj'} \|\Delta_g^{jj'} \Upsilon^{(r)}\|_q \\ & + \lambda_{1,n} \sum_{i=1}^t \sum_{j=1}^s \|\Upsilon_{[ij]}\|_1 + \lambda_{2,n} \sum_{i=1}^t \sum_{j=1}^s \|\Upsilon_{[ij]}\|_2.\end{aligned}$$

Our goal is to establish the consistency result of the estimator  $\widehat{\Theta}_n$  under the asymptotic regime  $n \rightarrow \infty$ . The following theorem shows that  $\widehat{\Theta}_n$  achieves  $\sqrt{n}$ -consistency. In particular, when the penalty parameters satisfy  $\lambda_{i,n} = o(\sqrt{n})$  for  $i \in 1, 2, t, g$ , the estimator  $\widehat{\Theta}_n$  converges in distribution to the true coefficient tensor  $\Theta$  in model (2) as  $n \rightarrow \infty$ .

**Theorem 1.** *Suppose Assumptions 1 and 2 hold. If  $\lambda_{i,n}/\sqrt{n} \rightarrow \lambda_{i,0} \geq 0$  for  $i = 1, 2, t, g$ . Then*

$$\sqrt{n}(\widehat{\Theta}_n - \Theta) \rightarrow \arg \min_{\zeta \in \mathbb{R}^{t \times s \times m}} F_\infty(\zeta)$$

in distribution as  $n \rightarrow \infty$ , where  $\Theta$  is the true coefficient tensor from model (2), and

$$\begin{aligned}F_\infty(\zeta) := & \sum_{r=1}^m \frac{1}{2} \left( \langle \zeta^{(r)}, \mathcal{M}(\zeta^{(r)}) \rangle - 2 \langle \zeta^{(r)}, \Xi^{(r)} \rangle \right) \\ & + \lambda_{t,0} \sum_{r=1}^m \sum_{i=1}^{t-1} \phi_{p, \Delta_t^i \Theta^{(r)}}(\Delta_t^i \zeta^{(r)}) + \lambda_{g,0} \sum_{r=1}^m \sum_{(j,j') \in \mathcal{E}} w_{jj'} \phi_{q, \Delta_g^{jj'} \Theta^{(r)}}(\Delta_g^{jj'} \zeta^{(r)}) \\ & + \lambda_{1,0} \sum_{i=1}^t \sum_{j=1}^s \phi_{1, \Theta_{[ij]}}(\zeta_{[ij]}) + \lambda_{2,0} \sum_{i=1}^t \sum_{j=1}^s \phi_{2, \Theta_{[ij]}}(\zeta_{[ij]}).\end{aligned}$$

with

$$\phi_{\alpha,v}(h) = \begin{cases} \sum_{k: v_k \neq 0} \text{sgn}(v_k) h_k + \sum_{k: v_k = 0} |h_k| & \text{if } \alpha = 1, \\ \mathbb{I}_{\{v \neq 0\}} v^\top h / \|v\|_2 + \mathbb{I}_{\{v = 0\}} \|h\|_2 & \text{if } \alpha = 2. \end{cases}$$

for any vectors  $v$  and  $h$  of the same length.

In particular, if  $\lambda_{i,n} = o(\sqrt{n})$  for  $i = 1, 2, t, g$ , then we have

$$\sqrt{n}(\widehat{\Theta}_n - \Theta) \rightarrow \arg \min_{\zeta \in \mathbb{R}^{t \times s \times m}} F_\infty(\zeta) = \bar{\zeta}$$

with  $\bar{\zeta}^{(r)} = \mathcal{M}^{-1} \Xi^{(r)}$  for  $r \in [m]$ , where  $\Xi^{(r)}$ 's are mean-zero Gaussian matrices satisfying (6).

*Proof.* Denote  $\widehat{\zeta}_n := \sqrt{n}(\widehat{\Theta}_n - \Theta)$  and define a function  $F_n : \mathbb{R}^{t \times s \times m} \rightarrow \mathbb{R}$  as

$$\begin{aligned} F_n(\zeta) &= \sum_{r=1}^m \frac{1}{2} \left( \|y^{(r)} - \mathcal{X}(\Theta^{(r)} + \zeta^{(r)}/\sqrt{n})\|_2^2 - \|y^{(r)} - \mathcal{X}(\Theta^{(r)})\|_2^2 \right) \\ &\quad + \lambda_{t,n} \sum_{r=1}^m \sum_{i=1}^{t-1} \left( \|\Delta_t^i \Theta^{(r)} + \Delta_t^i \zeta^{(r)}/\sqrt{n}\|_p - \|\Delta_t^i \Theta^{(r)}\|_p \right) \\ &\quad + \lambda_{g,n} \sum_{r=1}^m \sum_{(j,j') \in \mathcal{E}} w_{jj'} \left( \|\Delta_g^{jj'} \Theta^{(r)} + \Delta_g^{jj'} \zeta^{(r)}/\sqrt{n}\|_q - \|\Delta_g^{jj'} \Theta^{(r)}\|_q \right) \\ &\quad + \lambda_{1,n} \sum_{i=1}^t \sum_{j=1}^s \left( \|\Theta_{[ij]} + \zeta_{[ij]}/\sqrt{n}\|_1 - \|\Theta_{[ij]}\|_1 \right) \\ &\quad + \lambda_{2,n} \sum_{i=1}^t \sum_{j=1}^s \left( \|\Theta_{[ij]} + \zeta_{[ij]}/\sqrt{n}\|_2 - \|\Theta_{[ij]}\|_2 \right). \end{aligned}$$

By construction, we have

$$\arg \min_{\zeta \in \mathbb{R}^{t \times s \times m}} F_n(\zeta) = \widehat{\zeta}_n = \sqrt{n}(\widehat{\Theta}_n - \Theta).$$

First, by Taylor expansion, the smooth data-fitting term satisfies:

$$\begin{aligned} &\sum_{r=1}^m \frac{1}{2} \left( \|y^{(r)} - \mathcal{X}(\Theta^{(r)} + \zeta^{(r)}/\sqrt{n})\|_2^2 - \|y^{(r)} - \mathcal{X}(\Theta^{(r)})\|_2^2 \right) \\ &= \sum_{r=1}^m \frac{1}{2} \left( -2\langle \zeta^{(r)}, \Xi_n^{(r)} \rangle + \langle \zeta^{(r)}, \mathcal{M}_n(\zeta^{(r)}) \rangle \right) \\ &\rightarrow \sum_{r=1}^m \frac{1}{2} \left( -2\langle \zeta^{(r)}, \Xi^{(r)} \rangle + \langle \zeta^{(r)}, \mathcal{M}(\zeta^{(r)}) \rangle \right) \end{aligned}$$

in distribution as  $n \rightarrow \infty$ , using Assumptions 1 and 2.

Next, for vectors  $v$  and  $h$  of the same length, we have

$$\|v + h/\sqrt{n}\|_1 - \|v\|_1 = \frac{1}{\sqrt{n}} \sum_{k:v_k \neq 0} \text{sgn}(v_k) h_k + \frac{1}{\sqrt{n}} \sum_{k:v_k=0} |h_k| = \frac{1}{\sqrt{n}} \phi_{1,v}(h),$$

and also

$$\begin{aligned} \|v + h/\sqrt{n}\|_2 - \|v\|_2 &= \frac{1}{\sqrt{n}} \mathbb{I}_{\{v \neq 0\}} v^\top h / \|v\|_2 + \frac{1}{\sqrt{n}} \mathbb{I}_{\{v=0\}} \|h\|_2 + o\left(\frac{1}{\sqrt{n}}\right) \\ &= \frac{1}{\sqrt{n}} \phi_{2,v}(h) + o\left(\frac{1}{\sqrt{n}}\right), \end{aligned}$$

by Taylor expansion. Given the condition that  $\lambda_{i,n}/\sqrt{n} \rightarrow \lambda_{i,0}$  for  $i = 1, 2, t, g$ , we obtain the following component-wise convergence. For  $i \in [t]$ ,  $j \in [s]$ ,

$$\begin{aligned} \lambda_{1,n} (\|\Theta_{[ij]} + \zeta_{[ij]}/\sqrt{n}\|_1 - \|\Theta_{[ij]}\|_1) &\rightarrow \lambda_{1,0} \phi_{1,\Theta_{[ij]}}(\zeta_{[ij]}), \\ \lambda_{2,n} (\|\Theta_{[ij]} + \zeta_{[ij]}/\sqrt{n}\|_2 - \|\Theta_{[ij]}\|_2) &\rightarrow \lambda_{2,0} \phi_{2,\Theta_{[ij]}}(\zeta_{[ij]}), \end{aligned}$$

and for  $r \in [m]$ ,  $i \in [t-1]$ ,  $(j, j') \in \mathcal{E}$ ,

$$\begin{aligned} \lambda_{t,n} (\|\Delta_t^i \Theta^{(r)} + \Delta_t^i \zeta^{(r)}/\sqrt{n}\|_p - \|\Delta_t^i \Theta^{(r)}\|_p) &\rightarrow \lambda_{t,0} \phi_{p,\Delta_t^i \Theta^{(r)}}(\Delta_t^i \zeta^{(r)}), \\ \lambda_{g,n} (\|\Delta_g^{jj'} \Theta^{(r)} + \Delta_g^{jj'} \zeta^{(r)}/\sqrt{n}\|_q - \|\Delta_g^{jj'} \Theta^{(r)}\|_q) &\rightarrow \lambda_{g,0} \phi_{q,\Delta_g^{jj'} \Theta^{(r)}}(\Delta_g^{jj'} \zeta^{(r)}), \end{aligned}$$

as  $n \rightarrow \infty$ . Therefore,  $F_n(\zeta) \rightarrow F_\infty(\zeta)$  in distribution for every fixed  $\zeta \in \mathbb{R}^{t \times s \times m}$ .

Since  $F_\infty$  is strictly convex with a unique minimizer and  $F_n$  is convex, the convexity lemma [24] implies

$$\sqrt{n}(\widehat{\Theta}_n - \Theta) = \arg \min_{\zeta \in \mathbb{R}^{t \times s \times m}} F_n(\zeta) \rightarrow \arg \min_{\zeta \in \mathbb{R}^{t \times s \times m}} F_\infty(\zeta)$$

in distribution as  $n \rightarrow \infty$ . In particular, when  $\lambda_{i,0} = 0$  for  $i = 1, 2, t, g$ , the unique minimizer of  $F_\infty$  takes the explicit form:

$$\bar{\zeta} := \arg \min_{\zeta \in \mathbb{R}^{t \times s \times m}} F_\infty(\zeta)$$

with  $\bar{\zeta}^{(r)} = \mathcal{M}^{-1}\Xi^{(r)}$  for  $r \in [m]$ . This completes the proof.  $\square$

## 4 A Halpern Peaceman-Rachford Method

In this section, we employ the Halpern Peaceman–Rachford (HPR) method to solve the single-task learning problem (3) and its multi-task counterpart (5). Since the single-task model (3) arises as the special case of the multi-task model (5) with  $m = 1$  and  $\lambda_2 = 0$ , we focus on the latter problem.

For subsequent algorithmic development, it is convenient to rewrite (5) into the following compact form:

$$\min \ell(\Theta) + \Omega(\mathcal{P}\Theta) + \Phi(\mathcal{Q}\Theta) + \Psi(\Theta), \quad (7)$$

where the operators  $\mathcal{P}$ ,  $\mathcal{Q}$ , and the functions  $\ell, \Omega, \Phi, \Psi$  are introduced below. First, the squared loss function is given by

$$\ell(\Theta) = \frac{1}{2} \sum_{r=1}^m \|y^{(r)} - \mathcal{X}(\Theta^{(r)})\|_2^2,$$

for  $\Theta = [\Theta^{(1)}, \dots, \Theta^{(m)}] \in \mathbb{R}^{t \times s \times m}$ . Second, temporal smoothness is imposed by the  $(t-1) \times t$  difference matrix  $P \in \mathbb{R}^{(t-1) \times t}$ , based on which we define the linear operator  $\mathcal{P} : \mathbb{R}^{t \times s \times m} \rightarrow \mathbb{R}^{(t-1) \times s \times m}$ :

$$P = \begin{bmatrix} 1 & -1 & & & & \\ & 1 & -1 & & & \\ & & \ddots & \ddots & & \\ & & & & 1 & -1 \end{bmatrix}, \quad \mathcal{P}\Theta = [P\Theta^{(1)}, \dots, P\Theta^{(m)}].$$

The temporal regularizer  $\Omega : \mathbb{R}^{(t-1) \times s \times m} \rightarrow \mathbb{R}$  then takes the form

$$\Omega(W) = \lambda_t \sum_{r=1}^m \sum_{i=1}^{t-1} \|W_{i \cdot}^{(r)}\|_p, \quad W = [W^{(1)}, \dots, W^{(m)}].$$

Third, spatial smoothness is imposed by the node-arc incidence matrix of the spatial graph  $\mathcal{G} = ([s], \mathcal{E}, (w_{jj'}))$ . Let  $|\mathcal{E}|$  be the number of edges, indexed lexicographically via  $\iota : \mathcal{E} \rightarrow [| \mathcal{E} |]$ . The (unweighted) incidence matrix  $B \in \mathbb{R}^{s \times |\mathcal{E}|}$  and the linear operator  $\mathcal{Q} : \mathbb{R}^{t \times s \times m} \rightarrow \mathbb{R}^{t \times |\mathcal{E}| \times m}$  are defined by

$$B_{k, \iota(j, j')} = \begin{cases} 1, & k = j, \\ -1, & k = j', \\ 0, & \text{otherwise,} \end{cases} \quad \mathcal{Q}\Theta = [\Theta^{(1)}B, \dots, \Theta^{(m)}B].$$

The spatial regularizer  $\Phi : \mathbb{R}^{t \times |\mathcal{E}| \times m} \rightarrow \mathbb{R}$  is then

$$\Phi(Z) = \lambda_g \sum_{r=1}^m \sum_{j, j'} w_{jj'} \|Z_{\cdot \iota(j, j')}^{(r)}\|_q, \quad Z = [Z^{(1)}, \dots, Z^{(m)}].$$

Lastly, the cross-task sparse group Lasso regularizer is given by

$$\Psi(\Theta) = \sum_{i=1}^t \sum_{j=1}^s \left( \lambda_1 \|\Theta_{[ij]}\|_1 + \lambda_2 \|\Theta_{[ij]}\|_2 \right),$$

where the  $\ell_1$  term promotes sparsity at the element-wise level, and the  $\ell_2$  term encourages a shared sparsity support across tasks.

#### 4.1 An HPR Method for Solving MultiGGFL

To apply the HPR method, we rewrite problem (7) in an equivalent constrained form by introducing three sets of slack variables that separate the loss, temporal regularizer (slack variable  $W \in \mathbb{R}^{(t-1) \times s \times m}$ ), spatial regularizer (slack variable  $Z \in \mathbb{R}^{t \times |\mathcal{E}| \times m}$ ), and cross-task sparse group regularizer (slack variable  $U \in \mathbb{R}^{t \times s \times m}$ ). Specifically, we consider

$$\begin{aligned} \min \quad & \ell(\Theta) + \Omega(W) + \Phi(Z) + \Psi(U) \\ \text{s.t.} \quad & \mathcal{P}\Theta - W = 0, \quad \mathcal{Q}\Theta - Z = 0, \quad \Theta - U = 0. \end{aligned} \quad (8)$$

Let  $S \in \mathbb{R}^{(t-1) \times s \times m}$ ,  $T \in \mathbb{R}^{t \times |\mathcal{E}| \times m}$ , and  $R \in \mathbb{R}^{t \times s \times m}$  be the Lagrange multipliers associated with the three linear constraints. The KKT system associated with (8) for a primal-dual pair  $H := (\Theta, W, Z, U, S, T, R)$  is

$$\begin{aligned} 0 &= \nabla \ell(\Theta) + \mathcal{P}^* S + \mathcal{Q}^* T + R, \\ 0 &\in \partial \Omega(W) - S, \quad 0 \in \partial \Phi(Z) - T, \quad 0 \in \partial \Psi(U) - R, \\ \mathcal{P}\Theta - W &= 0, \quad \mathcal{Q}\Theta - Z = 0, \quad \Theta - U = 0. \end{aligned} \quad (9)$$

Since the primal problem (8) has a solution, it follows from [25, Corollary 28.3.1] that the KKT system admits a solution. For  $\sigma > 0$ , the augmented Lagrangian function associated with (8) is

$$\begin{aligned} \mathcal{L}_\sigma(\Theta, W, Z, U; S, T, R) &= \ell(\Theta) + \Omega(W) + \Phi(Z) + \Psi(U) \\ &+ \langle S, \mathcal{P}\Theta - W \rangle + \langle T, \mathcal{Q}\Theta - Z \rangle + \langle R, \Theta - U \rangle \\ &+ \frac{\sigma}{2} \left( \|\mathcal{P}\Theta - W\|_F^2 + \|\mathcal{Q}\Theta - Z\|_F^2 + \|\Theta - U\|_F^2 \right). \end{aligned}$$

Based on this setup, we now describe the HPR method for solving (8), summarized in Algorithm 1. Its global convergence follows from [17, Corollary 3.5]. For completeness, we state it in Theorem 2.

**Theorem 2.** *The sequence  $\{\bar{H}_k\} = \{(\bar{\Theta}_k, \bar{W}_k, \bar{Z}_k, \bar{U}_k, \bar{S}_k, \bar{T}_k, \bar{R}_k)\}$  generated by Algorithm 1 converges to  $H^* = (\Theta^*, W^*, Z^*, U^*, S^*, T^*, R^*)$ , which satisfies the KKT system (9). Namely,  $(\Theta^*, W^*, Z^*, U^*)$  is an optimal solution to problem (8), and  $(S^*, T^*, R^*)$  is an optimal solution to its dual problem.*

*Proof.* We first rewrite problem (8) in a standard two-block form [17, (1.1)]:

$$\min_{y, z} \quad f_1(y) + f_2(z) \quad \text{s.t.} \quad B_1 y + B_2 z = 0,$$

where  $f_1(y) := \Omega(W) + \Phi(Z) + \Psi(U)$ ,  $f_2(z) := \ell(\Theta)$ , with

$$y := \begin{bmatrix} W \\ Z \\ U \end{bmatrix}, \quad z := \Theta, \quad B_1 = -I, \quad B_2 = \begin{bmatrix} \mathcal{P} \\ \mathcal{Q} \\ I \end{bmatrix}.$$

Since both  $B_1^* B_1$  and  $B_2^* B_2$  are positive definite, Assumptions 1 and 2 in [17] hold. The global convergence then follows directly from [17, Corollary 3.5].  $\square$

---

**Algorithm 1** An HPR method for solving (8):  $(\bar{H}_{k+1}, k+1) = \mathbf{HPR}(H_0, \sigma)$ .

---

**Input:**  $H_0 = (\Theta_0, W_0, Z_0, U_0, S_0, T_0, R_0)$ ,  $\sigma > 0$ .

**for**  $k = 0, 1, \dots$  **do**

**Step 1.**  $\bar{\Theta}_{k+1} = \arg \min_{\Theta} \mathcal{L}_{\sigma}(\Theta, W_k, Z_k, U_k, S_k, T_k, R_k)$ .

**Step 2.** Update multipliers:

$$\begin{aligned}\bar{S}_{k+1} &= S_k + \sigma(\mathcal{P}\bar{\Theta}_{k+1} - W_k), \\ \bar{T}_{k+1} &= T_k + \sigma(\mathcal{Q}\bar{\Theta}_{k+1} - Z_k), \\ \bar{R}_{k+1} &= R_k + \sigma(\bar{\Theta}_{k+1} - U_k).\end{aligned}$$

**Step 3.** Update slack variables:

$$(\bar{W}_{k+1}, \bar{Z}_{k+1}, \bar{U}_{k+1}) = \arg \min_{W, Z, U} \mathcal{L}_{\sigma}(\bar{\Theta}_{k+1}, W, Z, U; \bar{S}_{k+1}, \bar{T}_{k+1}, \bar{R}_{k+1}).$$

**Step 4.** Extrapolation:  $\hat{H}_{k+1} = 2\bar{H}_{k+1} - H_k$ .

**Step 5.** Halpern iteration:

$$H_{k+1} = \frac{1}{k+2}H_0 + \frac{k+1}{k+2}\hat{H}_{k+1}.$$

**end for**

**Output:**  $(\bar{H}_{k+1}, k+1)$ .

---

**Remark 2.** Although Algorithm 1 follows the update steps of the accelerated preconditioned ADMM (pADMM) framework [17, Algorithm 3.1] with parameters  $\alpha = \rho = 2$  and  $\mathcal{T}_1 = \mathcal{T}_2 = 0$ , it has been shown in [16, Proposition 4] that pADMM with this parameter setting is mathematically equivalent to the HPR method in [15]. For this reason, we refer to Algorithm 1 as the HPR method throughout this paper.

We measure the convergence of Algorithm 1 via the KKT residual and the objective value gap. The residual mapping  $\mathcal{R}$  associated with the KKT system (9) is defined as:

$$\mathcal{R}(H) := \begin{pmatrix} \Theta - \text{prox}_{\ell}(\Theta - \mathcal{P}^*S - \mathcal{Q}^*T - R) \\ W - \text{prox}_{\Omega}(W + S) \\ Z - \text{prox}_{\Phi}(Z + T) \\ U - \text{prox}_{\Psi}(U + R) \\ \mathcal{P}\Theta - W \\ \mathcal{Q}\Theta - Z \\ \Theta - U \end{pmatrix},$$

for  $H = (\Theta, W, Z, U, S, T, R)$ . A point  $H^*$  satisfies (9) if and only if  $\mathcal{R}(H^*) = 0$ . We also measure the optimality gap for the objective function  $F(\Theta, W, Z, U) := \ell(\Theta) + \Omega(W) + \Phi(Z) + \Psi(U)$  in (8):

$$\Delta F(\bar{\Theta}_k, \bar{W}_k, \bar{Z}_k, \bar{U}_k) := F(\bar{\Theta}_k, \bar{W}_k, \bar{Z}_k, \bar{U}_k) - F(\Theta^*, W^*, Z^*, U^*),$$

where  $(\Theta^*, W^*, Z^*, U^*)$  denotes the limit point of the sequence  $\{(\bar{\Theta}_k, \bar{W}_k, \bar{Z}_k, \bar{U}_k)\}$  established in Theorem 2, and thus is an optimal solution of (8).

Based on [17, Theorem 3.7], Algorithm 1 achieves a non-ergodic  $\mathcal{O}(1/k)$  convergence rate, as stated below.

**Theorem 3.** Let  $\{\bar{H}_k\} = \{(\bar{\Theta}_k, \bar{W}_k, \bar{Z}_k, \bar{U}_k, \bar{S}_k, \bar{T}_k, \bar{R}_k)\}$  be the sequence generated by Algorithm 1, and let  $H^* = (\Theta^*, W^*, Z^*, U^*, S^*, T^*, R^*)$  be its limit point. Then for all  $k \geq 0$ , the following bounds hold:

$$\|\mathcal{R}(\bar{H}_k)\|_F \leq c \left(1 + \frac{1}{\sigma}\right) \frac{1}{k+1},$$

and

$$-\frac{cd}{\sigma} \frac{1}{k+1} \leq \Delta F(\bar{\Theta}_k, \bar{W}_k, \bar{Z}_k, \bar{U}_k) \leq \frac{(3c+d)c}{\sigma} \frac{1}{k+1},$$

where

$$c := \left\| \sigma \begin{pmatrix} W_0 - W^* \\ Z_0 - Z^* \\ U_0 - U^* \end{pmatrix} - \begin{pmatrix} S_0 - S^* \\ T_0 - T^* \\ R_0 - R^* \end{pmatrix} \right\|_F$$

measures the distance from the initial point to the limit point, and  $d = \|(S^*, T^*, R^*)\|_F$  is the norm of the optimal multipliers.

## 4.2 Per-iteration Updates and Costs

This subsection details the explicit update formulas and computational costs for each step of Algorithm 1.

Step 1 of Algorithm 1 can be solved by setting the gradient of  $\mathcal{L}_\sigma$  with respect to each  $\Theta^{(r)}$  to be zero. A direct calculation shows that each  $\bar{\Theta}_{k+1}^{(r)}$  can be computed by solving the linear system

$$\mathcal{X}^* \mathcal{X}(\bar{\Theta}_{k+1}^{(r)}) + \sigma(I_t + P^\top P)\bar{\Theta}_{k+1}^{(r)} + \sigma\bar{\Theta}_{k+1}^{(r)}(QQ^\top) = b_k^{(r)}, \quad (10)$$

where

$$b_k^{(r)} := \mathcal{X}^* y^{(r)} + P^\top (\sigma W_k^{(r)} - S_k^{(r)}) + (\sigma Z_k^{(r)} - T_k^{(r)})Q^\top + \sigma U_k^{(r)} - R_k^{(r)},$$

and  $\mathcal{X}^*$  denotes the adjoint of  $\mathcal{X}$ . We denote the temporal and spatial Laplacians as  $L_P = P^\top P$  and  $L_Q = QQ^\top$ , respectively, with their entries defined as:

$$(L_P)_{ii'} = \begin{cases} 2, & 2 \leq i = i' \leq t-1, \\ 1, & i = i' = 1 \text{ or } i = i' = t, \\ -1, & |i - i'| = 1, \\ 0, & \text{otherwise,} \end{cases} \quad (L_Q)_{jj'} = \begin{cases} \deg(v_j), & j' = j, \\ -1, & j' \neq j \text{ and } (j, j') \in \mathcal{E}, \\ 0, & \text{otherwise,} \end{cases}$$

where  $\deg(v_j)$  denotes the degree of vertex  $v_j$  in the spatial graph  $\mathcal{G}$ . Vectorizing (10) yields the linear system

$$(X^\top X + \sigma I_s \otimes (I_t + L_P) + \sigma L_Q \otimes I_t) \text{vec}(\bar{\Theta}_{k+1}^{(r)}) = \text{vec}(b_k^{(r)}), \quad (11)$$

where  $X = [\text{vec}(X_1), \text{vec}(X_2), \dots, \text{vec}(X_n)]^\top \in \mathbb{R}^{n \times ts}$ . It can be solved efficiently by direct solvers (e.g., Cholesky factorization for small or medium scales) or iterative solvers such as the conjugate gradient method.

In Step 3, the variables  $\mathcal{W}$ ,  $\mathcal{Z}$ , and  $\mathcal{U}$  are updated via the following proximal mappings:

$$\begin{aligned} \bar{W}_{k+1} &= \text{prox}_{\Omega/\sigma}(\mathcal{P}\bar{\Theta}_{k+1} + \sigma^{-1}\bar{S}_{k+1}), \\ \bar{Z}_{k+1} &= \text{prox}_{\Phi/\sigma}(\mathcal{Q}\bar{\Theta}_{k+1} + \sigma^{-1}\bar{T}_{k+1}), \\ \bar{U}_{k+1} &= \text{prox}_{\Psi/\sigma}(\bar{\Theta}_{k+1} + \sigma^{-1}\bar{R}_{k+1}), \end{aligned}$$

which admit closed-form solutions. For  $\nu > 0$ ,  $U \in \mathbb{R}^{t \times s \times m}$ ,  $W \in \mathbb{R}^{(t-1) \times s \times m}$ , and  $Z \in \mathbb{R}^{t \times |\mathcal{E}| \times m}$ , they are given by

$$\begin{aligned} [\text{prox}_{\Omega/\sigma}(W)]_{i \cdot}^{(r)} &= \text{prox}_{\lambda_t/\sigma \|\cdot\|_p} \left( W_{i \cdot}^{(r)} \right), \\ [\text{prox}_{\Phi/\sigma}(Z)]_{\cdot i(j,j')}^{(r)} &= \text{prox}_{\lambda_g w_{jj'} / \sigma \|\cdot\|_q} \left( Z_{\cdot i(j,j')}^{(r)} \right), \\ [\text{prox}_{\Psi/\sigma}(U)]_{[ij]} &= \text{prox}_{\lambda_2/\sigma \|\cdot\|_2} \left( \text{prox}_{\sigma^{-1}\lambda_1 \|\cdot\|_1} (U_{[ij]}) \right). \end{aligned}$$

With these update rules, we are ready to quantify the computational cost of one loop of Algorithm 1. First, a one-time preprocessing step is required to form the coefficient matrix  $X^\top X + \sigma I_s \otimes (I_t + L_P) + \sigma L_Q \otimes I_t \in \mathbb{S}^{ts}$  and the vectors  $\{\mathcal{X}^* y^{(r)} \mid r \in [m]\}$  appearing on the right-hand side of the linear system (11). These computations require  $\mathcal{O}(t^2 s^2 n)$  and  $tsmn$  operations, respectively. Subsequently, factorizing the resulting  $ts \times ts$  matrix using the Cholesky decomposition incurs additional  $\mathcal{O}(t^3 s^3)$  operations. Next, within each iteration of Algorithm 1, the right-hand side  $b_k^{(r)}$  of the linear system (11) can be formed in  $\mathcal{O}(ts + t|\mathcal{E}|)$  operations for each  $r \in [m]$ , and solving the system using the precomputed Cholesky factors then costs  $\mathcal{O}(t^2 s^2)$  operations per right-hand side. Thus, Step 1 of Algorithm 1 requires  $\mathcal{O}(tsm + t|\mathcal{E}|m + t^2 s^2 m)$  operations per loop. The remaining proximal updates for  $W$ ,  $Z$ , and  $U$  are lightweight, each costing at most  $\mathcal{O}(tsm + t|\mathcal{E}|m)$ , which is dominated by the linear-system solve. In summary, the dominant computational cost in each loop of Algorithm 1 comes from solving the linear system in Step 1, which requires  $\mathcal{O}(tsm + t|\mathcal{E}|m + t^2 s^2 m)$  operations, while all remaining updates contribute only lower-order costs.

### 4.3 Practical Acceleration

To enhance practical efficiency, we incorporate two strategies from [16, 18]: a restart mechanism that adaptively reinitializes the sequence to accelerate convergence, and an adaptive  $\sigma$  update that dynamically balances the primal and dual residuals.

First, we monitor the progress of the  $(k+1)$ -th iteration via the residual quantity:

$$c_k := \left\| \sigma \begin{pmatrix} \widehat{W}_{k+1} - W_k \\ \widehat{Z}_{k+1} - Z_k \\ \widehat{U}_{k+1} - U_k \end{pmatrix} - \begin{pmatrix} \widehat{S}_{k+1} - S_k \\ \widehat{T}_{k+1} - T_k \\ \widehat{R}_{k+1} - R_k \end{pmatrix} \right\|_F.$$

We check  $c_k$  every 50 iterations, and the HPR loop terminates (restarts) if any of the following hold:

$$\begin{aligned} c_{k-1} < c_k \leq \alpha_1 c_0, & \quad \alpha_1 \in (0, 1), \\ c_k \leq \alpha_2 c_0, & \quad \alpha_2 \in (0, \alpha_1), \\ k \geq \alpha_3 t, & \quad \alpha_3 > 0. \end{aligned} \tag{12}$$

In our experiments, we set  $\alpha_1 = 0.6$ ,  $\alpha_2 = 0.2$ , and  $\alpha_3 = 0.25$ . The three conditions trigger a restart when:  $c_k$  stops decaying (local stagnation);  $c_k$  drops sufficiently (successful decay); or the inner iteration count  $k$  becomes excessive relative to the total history  $t$ .

Upon restart, we update  $\sigma$  to balance primal and dual progress. We measure the relative motion of the primal and dual variables by

$$\Delta_p := \left\| \begin{pmatrix} \overline{W}_{\kappa+1} - \overline{W}_\kappa \\ \overline{Z}_{\kappa+1} - \overline{Z}_\kappa \\ \overline{U}_{\kappa+1} - \overline{U}_\kappa \end{pmatrix} \right\|_F, \quad \Delta_d := \left\| \begin{pmatrix} \overline{S}_{\kappa+1} - \overline{S}_\kappa \\ \overline{T}_{\kappa+1} - \overline{T}_\kappa \\ \overline{R}_{\kappa+1} - \overline{R}_\kappa \end{pmatrix} \right\|_F, \tag{13}$$

and set  $\sigma_{\kappa+1} = \Delta_d / \Delta_p$ . This practical implementation is summarized in Algorithm 2.

---

**Algorithm 2** Practical HPR for solving (8)

---

- 1: **Input:**  $\bar{H}_0$ ,  $\sigma_0 = 1$ . Set total iteration count  $t \leftarrow 0$ .
- 2: **for** outer iteration  $\kappa = 0, 1, \dots$  **do**
- 3:   **Step 1.** Run  $(\bar{H}_{\kappa+1}, \Delta t) \leftarrow \mathbf{HPR}(\bar{H}_\kappa, \sigma_\kappa)$ , checking conditions in (12) every 50 iterations. Terminate when met.
- 4:   **Step 2.** Set  $\sigma_{\kappa+1} \leftarrow \Delta_d / \Delta_p$ , and  $t \leftarrow t + \Delta t$ , where  $\Delta_d, \Delta_p$  are computed via (13).
- 5: **end for**
- 6: **Output:**  $\bar{H}_{\kappa+1}$ .

---

## 5 Numerical Experiments

In this section, we conduct extensive numerical experiments designed to examine both the statistical and computational aspects of our proposed estimators, compared with the state-of-the-art GTV and its variant [6–8]. We first evaluate their statistical behavior through simulation studies. Next, we investigate the computational efficiency and scalability of the proposed HPR algorithm in both single- and multi-task settings. Finally, we demonstrate the practical utility of our estimators in a real application on winter precipitation forecasting in the Southwestern United States (SWUS).

Experiments were conducted in MATLAB R2024a on an Intel i7-860 (2.80 GHz) CPU with 16 GB RAM. Unless otherwise noted, Algorithm 2 terminates if the total iteration count reaches 2000 or the normalized KKT residual satisfies:

$$\eta_{\text{KKT}} := \max\{R_d, R_p\} \leq 10^{-4},$$

where the primal ( $R_p$ ) and dual ( $R_d$ ) residuals are defined as:

$$\begin{aligned} R_p &= \max \left\{ \frac{\|\mathcal{P}\bar{\Theta}_\kappa - \bar{W}_\kappa\|_F}{1 + \|\bar{W}_\kappa\|_F}, \frac{\|\mathcal{Q}\bar{\Theta}_\kappa - \bar{Z}_\kappa\|_F}{1 + \|\bar{Z}_\kappa\|_F}, \frac{\|\bar{\Theta}_\kappa - \bar{U}_\kappa\|_F}{1 + \|\bar{U}_\kappa\|_F} \right\}, \\ R_d &= \max \left\{ \frac{\|\nabla \ell(\bar{\Theta}_\kappa) + \mathcal{P}^* \bar{S}_\kappa + \mathcal{Q}^* \bar{T}_\kappa + \bar{R}_\kappa\|_F}{1 + \|\bar{R}_\kappa\|_F}, \frac{\|\bar{W}_\kappa - \text{prox}_\Omega(\bar{W}_\kappa + \bar{S}_\kappa)\|_F}{1 + \|\bar{W}_\kappa\|_F}, \right. \\ &\quad \left. \frac{\|\bar{Z}_\kappa - \text{prox}_\Phi(\bar{Z}_\kappa + \bar{T}_\kappa)\|_F}{1 + \|\bar{Z}_\kappa\|_F}, \frac{\|\bar{U}_\kappa - \text{prox}_\Psi(\bar{U}_\kappa + \bar{R}_\kappa)\|_F}{1 + \|\bar{U}_\kappa\|_F} \right\}. \end{aligned}$$

In our experiments, we consider a setting where the  $s$  spatial locations lie on an  $s_1 \times s_2$  grid ( $s = s_1 s_2$ ). For simplicity, we set the weights in our models (3) and (5) to reflect 4-neighbor connectivity:

$$w_{jj'} = \begin{cases} 1, & \text{if } j \text{ and } j' \text{ are adjacent,} \\ 0, & \text{otherwise,} \end{cases} \quad (14)$$

which connect immediate horizontal and vertical neighbors in the spatial space.

### 5.1 Synthetic Data

We first compare the performance of the GGFL estimator with that of GTV [8], and then assess the computational scalability of the HPR algorithm (Algorithm 2) as the dimensions of the problem increase.

#### 5.1.1 Data Generation

We start by detailing the data generation process, which incorporates two key characteristics: first, the  $s$  spatial locations form a  $\sqrt{s} \times \sqrt{s}$  grid where adjacent locations exhibit similar behavior; second, the temporal evolution is smooth, interrupted by a single change point.

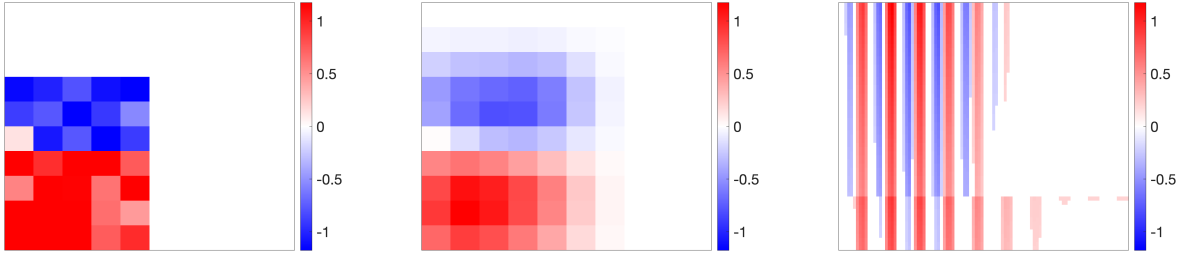


Figure 3: Illustration of a  $10 \times 10$  spatial grid for  $S$  (left) and  $\hat{S}$  (middle). Right: true coefficient matrix  $\theta \in \mathbb{R}^{60 \times 100}$ .

We consider the single-response model (1), with noise terms generated independently as  $\varepsilon_k \stackrel{\text{i.i.d.}}{\sim} \mathcal{N}(0, 10^{-4})$ . The predictors  $\{X_k\}_{k=1}^n$  are generated from a matrix-variate Gaussian distribution [26–28] as  $\text{vec}(X_k) \stackrel{\text{i.i.d.}}{\sim} \mathcal{N}(0, \Sigma_s \otimes \Sigma_t)$ ,  $k \in [n]$ . The temporal covariance  $\Sigma_t \in \mathbb{S}^t$  is defined by  $(\Sigma_t)_{ii'} = 0.9^{|i-i'|}$ , while the spatial covariance is block-diagonal:  $\Sigma_s = \text{diag}(\Sigma_0, \dots, \Sigma_0) \in \mathbb{S}^s$  with  $\Sigma_0 = 0.4I + 0.6\mathbf{1}\mathbf{1}^\top \in \mathbb{S}^{\sqrt{s}}$ , where  $\mathbf{1} \in \mathbb{R}^{\sqrt{s}}$  denotes the vector of all ones. The true coefficient matrix  $\theta \in \mathbb{R}^{t \times s}$  evolves over time from an initial state  $\theta_1$  according to:

$$\theta_i = 0.99\theta_{i-1} + \begin{cases} 0.2 & \text{if } i = t^* \\ 0 & \text{if } i \neq t^* \end{cases}, \quad \text{for } i = 2, \dots, t,$$

where the change point  $t^*$  is sampled uniformly from  $\{3, \dots, t-2\}$ . We construct  $\theta_1$  from a latent spatial matrix  $S \in \mathbb{R}^{\sqrt{s} \times \sqrt{s}}$ . The grid is partitioned into six roughly equal regions ( $3 \times 2$  layout). Entries in the middle-left and lower-left blocks are drawn from  $\mathcal{N}(1, 0.1)$  and  $\mathcal{N}(-1, 0.1)$ , respectively, while the remaining four regions are set to zero (see the left panel of Fig. 3). To avoid sharp spatial discontinuities, we apply Gaussian smoothing (see Fig. 3, middle panel) to  $S$  as

$$\hat{S}_{pq} = \frac{1}{2\pi} \sum_{p',q'} \exp\left(-\frac{(p-p')^2 + (q-q')^2}{2}\right) S_{p'q'}.$$

The initial coefficient is then defined as  $\theta_1 = \text{vec}(\hat{S})^\top$ . After generating the full coefficient  $\theta$  via the above temporal evolution, we threshold entries  $\theta_{ij}$  with magnitude below 0.2 to zero. The resulting true coefficient matrix  $\theta$  is shown in the right panel of Fig. 3.

For each instance, we generate independent training, validation, and test sets with sample sizes  $n$  (to be defined in the following subsections),  $n_{\text{val}} = 10^3$ , and  $n_{\text{test}} = 10^3$ , respectively.

### 5.1.2 Evaluation Performance

We compare our GGFL estimator (3), together with its simplified variant S-GGFL (which enforces  $\lambda_t = \lambda_g$  in (3) to reduce tuning time), against the state-of-the-art GTV estimator [8] defined in (4). For all three methods, regularization parameters are selected by minimizing the validation root mean squared error (RMSE). During the parameter tuning phase, each candidate configuration for GGFL and S-GGFL is solved by applying Algorithm 2 with the stopping criterion  $\eta_{\text{KKT}} \leq 10^{-3}$ .

To evaluate the performance of an estimator  $\hat{\theta}$  of the true coefficient  $\theta$ , we report the following prediction and estimation errors:

$$\text{RMSE-}y = \sqrt{\|\mathcal{X}_{\text{test}}(\hat{\theta}) - y_{\text{test}}\|_2^2 / n_{\text{test}}}, \quad \text{Error-}\theta = \frac{\|\hat{\theta} - \theta\|_2}{1 + \|\theta\|_2},$$

where  $\{(X_k^{\text{test}}, y_k^{\text{test}})\}_{k=1}^{n_{\text{test}}}$  denotes the test set and

$$\mathcal{X}_{\text{test}}(\theta) := [\langle X_1^{\text{test}}, \theta \rangle, \dots, \langle X_{n_{\text{test}}}^{\text{test}}, \theta \rangle]^\top.$$

We fix dimensions  $t = 90$ ,  $s = 100$  and vary the training sample size  $n \in \{100, 200, 500, 1000\}$ . Regularization parameters are tuned over grids of five logarithmically spaced values:  $\lambda_t, \lambda_g \in [10^{-2}, 10^2]$ ,  $\lambda_1 \in [10^{-4}, 10^{-2}]$  for GGFL/S-GGFL; and  $\lambda_1 \in [10^{-4}, 10^{-1}]$ ,  $\lambda_{tv} \in [10^{-4}, 10^{-2}]$  for GTV. Since GTV (4) requires an estimated covariance matrix  $\Sigma \in \mathbb{S}_+^{ts}$ , we generate an additional  $10^4$  independent samples to compute the sample covariance, applying entrywise thresholding at 0.5 following [8].

Table 1: Performance Comparison of Single-Task Estimators on Synthetic Data across Varying Training Sample Sizes  $n$

$n$	Estimator	RMSE- $y$	Error- $\theta$	Tuning Time	Final Fitting Time
100	S-GGFL	2.04e+01	3.12e-01	00:07:57	00:00:16
	GGFL	1.38e+01	2.12e-01	01:34:06	00:00:35
	GTV	7.70e+01	1.13e+02	02:09:07	00:02:34
200	S-GGFL	9.17e+00	1.60e-01	00:10:00	00:00:18
	GGFL	5.88e+00	1.11e-01	00:59:40	00:00:27
	GTV	5.53e+01	1.19e+02	02:58:04	00:04:27
500	S-GGFL	1.55e+00	5.32e-02	00:10:31	00:00:18
	GGFL	1.31e+00	4.85e-02	00:59:18	00:00:25
	GTV	1.26e+01	1.00e+02	04:24:30	00:01:56
1000	S-GGFL	3.36e-01	2.22e-02	00:09:20	00:00:20
	GGFL	3.36e-01	2.22e-02	00:55:17	00:00:20
	GTV	6.30e-01	1.03e+02	10:02:41	00:06:31

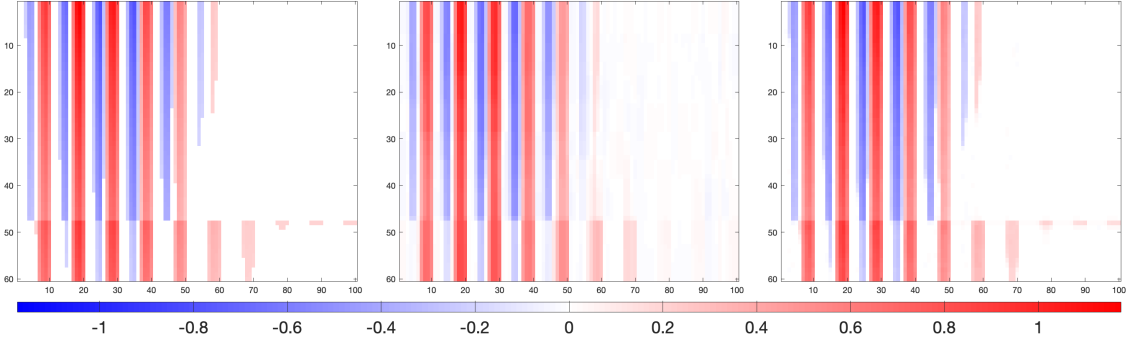


Figure 4: True coefficient matrix  $\theta$  (left), and GGFL estimated coefficient matrices with sample sizes  $n = 200$  (middle) and  $n = 1000$  (right).

Table 1 reports the test RMSE- $y$ , Error- $\theta$ , parameter tuning time, and final fitting time (using the selected optimal parameters) of three methods. The results show that GGFL consistently achieves the lowest RMSE- $y$  and Error- $\theta$ . For example, at  $n = 500$ , GGFL completes tuning and fitting in one hour and reaches RMSE- $y = 1.31$  and Error- $\theta = 4.85 \times 10^{-2}$ , whereas GTV requires over 4 hours, yielding significantly higher errors (12.6 and  $1 \times 10^2$ ). The simplified variant S-GGFL also performs remarkably well. At  $n = 1000$ , it requires only 10 minutes to achieve the same accuracy as GGFL, far outperforming GTV. Notably, while GTV uses  $10^4$  additional samples for covariance estimation, our estimators attain superior accuracy without this extra data, demonstrating that explicitly enforcing spatiotemporal structure offers a highly

effective alternative to covariance-based modeling.

Computationally, S-GGFL and GGFL demonstrate superior efficiency and scalability. As the sample size  $n$  increases, the tuning time of GTV increases from about 2 hours to more than 10 hours, while S-GGFL consistently completes the tuning within 10 minutes and the tuning time of GGFL decreases from 2 hours to 55 minutes. A similar trend is observed for fitting time: both GGFL and S-GGFL consistently finish within 1 minute, whereas GTV requires over 5 minutes at  $n = 1000$ . These results provide strong evidence that our methods are both efficient and effective compared with GTV.

Furthermore, we visualize the effect of sample size on the GGFL estimator. As shown in Fig. 4, when  $n = 200$ , the GGFL estimate shows non-negligible deviations in regions that are zero in the ground truth, reflecting limited-sample effects. In contrast, for  $n = 1000$ , these deviations vanish and the estimated pattern closely matches the ground truth, demonstrating a substantial decrease in estimation error as the sample size grows.

Overall, S-GGFL offers a well-balanced trade-off between accuracy and efficiency, making it particularly attractive in practice.

### 5.1.3 Computational Performance

We assess the computational scalability of the HPR algorithm (Algorithm 2) for solving (3) as the temporal length  $t$  and spatial dimension  $s$  increase. We further evaluate its scalability in the multi-task setting (5) by varying the number of tasks  $m$ , along with  $t$  and  $s$ . For the multi-task experiments, data are generated from the multi-task model (2), where the coefficient matrix  $\Theta^{(r)}$  for each task is constructed as Section 5.1.1 with all tasks sharing a common temporal change point  $t^*$ .

We first evaluate the scalability of the HPR algorithm for solving the single-task GGFL model with sample size  $n = 500$  by varying the temporal length  $t$  and spatial dimension  $s$ . Specifically, we consider  $t \in [60, 240]$  with  $s = 100$  fixed, and  $s \in [100, 400]$  with  $t = 60$  fixed. The results are shown in Fig. 5. We then conduct analogous experiments for the multi-task setting (MultiGGFL) with  $m = 5$ , varying  $t$  and  $s$  under the same settings, see the upper and middle panels of Fig. 6. We further assess the scalability with respect to the number of tasks by increasing  $m \in [5, 25]$  while fixing  $n = 500, t = 60, s = 100$  (Fig. 6, lower panel). In all experiments, we test four regularization strengths  $\lambda_0 \in \{10^{-3}, 10^{-2}, 10^{-1}, 1\}$ , setting all penalty parameters equal to  $\lambda_0$  (i.e.,  $\lambda_i = \lambda_0, i = 1, 2, t, g$ ).

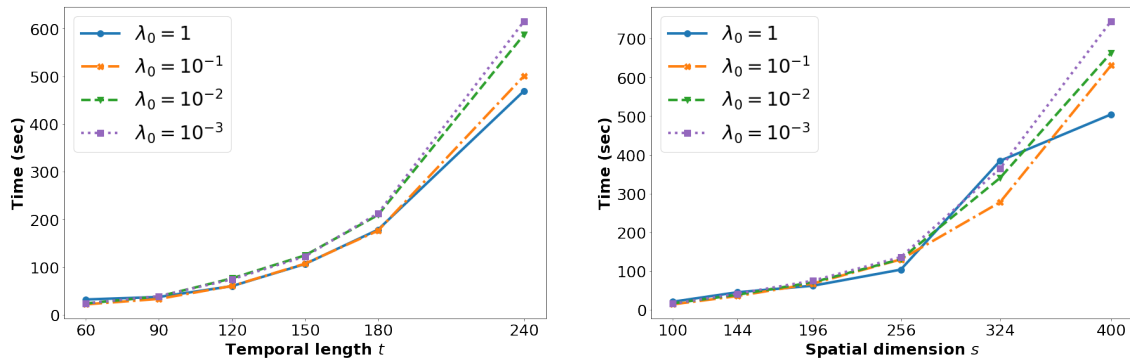


Figure 5: Runtime of HPR for GGFL under varying regularization strengths  $\lambda_0$ . Upper: Scaling with temporal length  $t$  (fixed  $n = 500, s = 100$ ). Lower: Scaling with spatial dimension  $s$  (fixed  $n = 500, t = 60$ ).

We can see from the figures that the computational time scales approximately linearly with  $m$  and at most quadratically with  $t$  and  $s$ , consistent with the complexity analysis in Section 4.2. Notably, the performance is generally insensitive to regularization strength, with

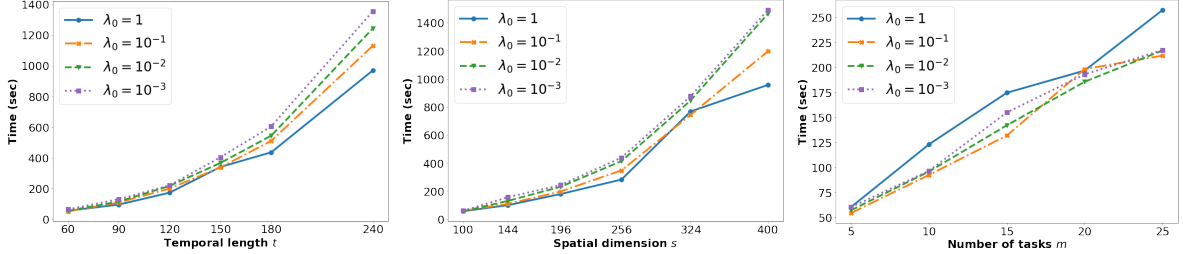


Figure 6: Runtime of HPR for MultiGGFL under varying regularization strengths  $\lambda_0$ . Upper: Scaling with temporal length  $t$  (fixed  $n = 500, s = 100, m = 5$ ). Middle: Scaling with spatial dimension  $s$  (fixed  $n = 500, t = 60, m = 5$ ). Lower: Scaling with number of tasks  $m$  (fixed  $n = 500, t = 60, s = 100$ ).

negligible runtime differences across different  $\lambda_0$ . These findings confirm that the HPR algorithm is robust and stable across varying problem dimensions and regularization strengths.

## 5.2 SWUS Precipitation Forecasting: Single-Task

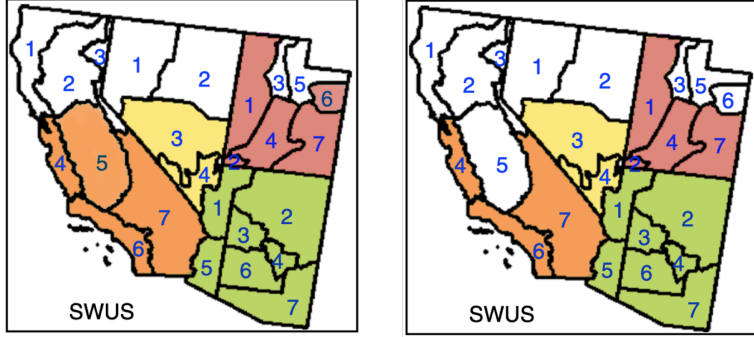


Figure 7: Illustration of selected SWUS climate divisions. Left: Divisions used to compute the area-weighted average winter precipitation response. Right: The 16 distinct divisions, each corresponding to a separate task in the multi-task setting. Regions are color-coded by state: California (orange), Nevada (yellow), Utah (red), and Arizona (green).

We evaluate the GGFL (3) and GTV (4) models for forecasting winter (November–March) precipitation in the southwestern United States (SWUS). Following the setup in [8], the dataset covers the period 1940–2018. For each year  $k$ , the response  $y_k$  is the area-weighted average winter precipitation over selected SWUS climate divisions (see Fig. 7, left panel). The predictor  $X_k \in \mathbb{R}^{t \times s}$  consists of sea surface temperatures (SST) from the preceding  $t = 4$  months (July–October) across  $s = 220$  spatial locations on a  $10^\circ \times 10^\circ$  grid over the Pacific ocean. In our experiment, we use preprocessed data from the GTV package<sup>1</sup>.

We partition the data into training (1940–1989,  $n = 50$ ) and testing (1990–2018,  $n_{\text{test}} = 29$ ) sets. During training, we replace the standard squared  $\ell_2$ -loss in (3) and (4) by a temporally weighted least squares to prioritize recent observations:

$$\|D^{\frac{1}{2}}(y - \mathcal{X}(\theta))\|_2^2, \text{ with } D = \text{diag}(\{0.9^{1989-k}\}_{k=1940}^{1989}). \quad (15)$$

Parameters are selected via five-fold cross-validation on the training set. We tune  $\lambda_1 \in [10^{-4}, 10^{-2}]$  and  $\lambda_t = \lambda_g \in [10^{-3}, 10^2]$  for GGFL, and  $\lambda_1 \in [10^{-4}, 10^{-1}]$  and  $\lambda_{tv} \in [10^{-4}, 10^{-2}]$  for GTV, using 20 logarithmically spaced values for each parameter. This parameter tuning for GTV covers a broader and finer range than that used in the GTV package [8].

<sup>1</sup>[https://github.com/Willett-Group/gtv\\_forecasting](https://github.com/Willett-Group/gtv_forecasting)

Since GTV requires a covariance estimate  $\Sigma \in \mathbb{S}^{ts}$ , we evaluate two variants: GTV(Obs), using the sample covariance computed directly from the training predictors; and GTV(LENS), using external data from the CESM Large Ensemble dataset [29] following [8]. Both variants apply a threshold of 0.5 to  $\Sigma$  to control graph sparsity.

Table 2: Forecasting Comparison for SWUS Winter Precipitation

Estimator	Test RMSE- $y$	Tuning Time	Fitting Time
GGFL	0.904	00:12:00	00:00:01
GTV(LENS)	0.983	00:43:49	00:00:02
GTV(Obs)	1.076	01:00:24	00:00:02

Table 2 summarizes the forecasting results. As can be seen, GGFL achieves the lowest test RMSE- $y$  (0.904), outperforming GTV(LENS) (0.983) and GTV(Obs) (1.076). We note that [8] reported a lower RMSE- $y$  of 0.860 for GTV(LENS), achieved via a specific selection of hyperparameter candidates. This discrepancy likely stems from the sensitivity of GTV to hyperparameter choices in limited-data regimes. Consistent with [8], GTV(LENS) outperforms GTV(Obs), confirming that incorporating external data improves covariance estimation. Computationally, GGFL is significantly more efficient, completing tuning in 12 minutes compared to 44 minutes for GTV(LENS) and 1 hour for GTV(Obs). These results show that GGFL consistently outperforms GTV in both predictive accuracy and computational efficiency.

### 5.3 SWUS Precipitation Forecasting: Multi-Task

For the multi-task experiments, we evaluate the performance under both joint (multi-task) and independent (single-task) settings. We compare MultiGGFL (5) against MultiGTV [6, (3)], which minimizes:

$$\begin{aligned} \min_{\Theta \in \mathbb{R}^{t \times s \times m}} \quad & \sum_{r=1}^m \left[ \|y^{(r)} - \mathcal{X}(\Theta^{(r)})\|_2^2 + \lambda_1 \|\Theta^{(r)}\|_1 + \lambda_1 \sum_{(i,j),(i',j')} |\Sigma_{(i,j),(i',j')}|^{\frac{1}{2}} |\Theta_{ij}^{(r)} - s_{(ij),(i'j')} \Theta_{i'j'}^{(r)}| \right] \\ & + \lambda_2 \sum_{i=1}^t \sum_{j=1}^s \|\Theta_{[ij]}\|_2. \end{aligned}$$

In the single-task setting, GGFL (3) and GTV (4) are fitted independently to each task.

In this setup, we define  $m = 16$  tasks corresponding to 16 SWUS climate divisions shown in the right panel of Fig. 7. The response  $y_k^{(r)}$  is the winter precipitation for division  $r$ , sourced from NOAA<sup>2</sup>, as divisional precipitation data are not included in the GTV package. Predictors  $X_k$  remain identical to the single-task setting. Data partitioning and the temporal weighting scheme of the loss also follow the protocol described in the previous subsection.

Parameters are tuned via five-fold cross-validation. For MultiGGFL, we select  $\lambda_1 = \lambda_2$  from 20 logarithmically spaced values in  $[10^{-4}, 10^{-2}]$ , and  $\lambda_t = \lambda_g$  from 20 values in  $[10^{-3}, 10^2]$ . For MultiGTV,  $\lambda_1$  and  $\lambda_2$  are tuned over 10 logarithmically spaced values in  $[10^{-3}, 10^2]$ . Due to the high computational cost of MultiGTV, we restrict the grid size and cap the runtime at 1800 seconds per instance.

Fig. 8 reports test RMSE- $y$  by division for all four models. The two GGFL variants achieve consistently lower test errors than their GTV counterparts, both across most divisions and on average. This highlights the advantage of explicitly enforcing temporal smoothness across consecutive time points and spatial similarity among adjacent regions. Although GGFL performs

<sup>2</sup><https://www.ncei.noaa.gov/pub/data/cirs/climdiv/> (dataset climdiv-pcpndv-v1.0.0-20250905)

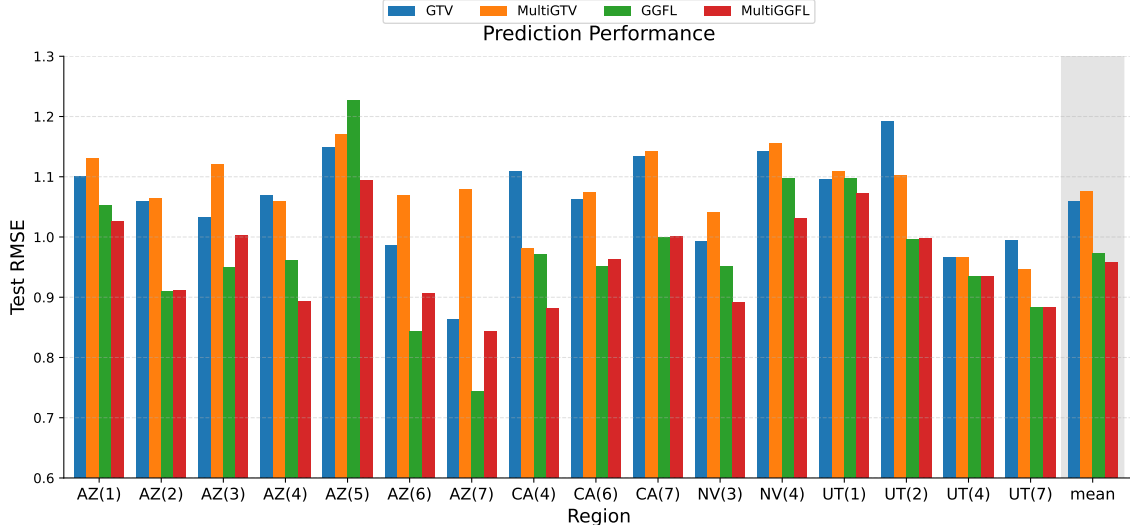


Figure 8: Forecasting comparison for SWUS winter precipitation across 16 divisions. The rightmost bar denotes the mean across all divisions. Computational times (Tuning / Fitting): GTV (10 hours / 2 minutes), MultiGTV (72 hours / 30 minutes), GGFL (3 hours / 20 seconds), and MultiGGFL (3 hours / 14 seconds).

competitively overall, it exhibits higher variance across divisions. For instance, it achieves the best results in AZ(6) and AZ(7), but performs the worst in AZ(5). In contrast, MultiGGFL attains the lowest mean RMSE- $y$  and exhibits smaller variability, showing that jointly learning across related tasks enhances both stability and accuracy. MultiGTV also improves upon GTV via task coupling but remains inferior to MultiGGFL. Computationally, both GGFL and MultiGGFL complete tuning and fitting within 3 hours. In contrast, GTV requires nearly 10 hours, and MultiGTV spans nearly 3 days. These results demonstrate that the proposed framework provides robust and efficient precipitation forecasting, with the multi-task formulation offering the greatest overall gains.

## 6 Conclusion

We present a unified framework for spatiotemporal matrix regression in single- and multi-task settings. Our GGFL estimator leverages a weighted spatial graph to couple neighboring locations while simultaneously enforces temporal smoothness and feature sparsity. Building on this, the multi-task extension further aligns structure across related tasks. On the theoretical front, we establish  $\sqrt{n}$ -consistency for our estimators. On the computational side, we employ the HPR algorithm for solving the resulting composite convex problem with a non-ergodic  $\mathcal{O}(1/k)$  rate and low per-iteration complexity, making the approach practical at scale. Numerical results indicate that the proposed methods show superior predictive performance and estimation accuracy compared with the state-of-the-art GTV estimators, while maintaining strong efficiency and scalability. These findings validate that our estimators offer a robust and interpretable route to high-dimensional spatiotemporal learning.

Several directions need further investigation. First, our framework could incorporate robust or generalized losses (e.g., Huber, logistic, or Poisson), allowing for the handling of heavy tails, outliers, and categorical data for classification. Second, rather than pre-specifying structures, adaptively learning spatiotemporal graphs from data [30] presents a promising avenue. Finally, exploring second-order information may further accelerate computation, offering a more efficient alternative for large-scale problems.

## References

- [1] R. Tibshirani, “Regression shrinkage and selection via the Lasso,” *Journal of the Royal Statistical Society Series B: Statistical Methodology*, vol. 58, no. 1, pp. 267–288, 1996.
- [2] R. Tibshirani, M. Saunders, S. Rosset, J. Zhu, and K. Knight, “Sparsity and smoothness via the fused Lasso,” *Journal of the Royal Statistical Society Series B: Statistical Methodology*, vol. 67, no. 1, pp. 91–108, 2005.
- [3] M. Yuan and Y. Lin, “Model selection and estimation in regression with grouped variables,” *Journal of the Royal Statistical Society Series B: Statistical Methodology*, vol. 68, no. 1, pp. 49–67, 2006.
- [4] J. Chen, Y. Wang, and M. K. Ng, “Quantized low-rank multivariate regression with random dithering,” *IEEE Transactions on Signal Processing*, vol. 71, pp. 3913–3928, 2023.
- [5] Y. Li, B. Mark, G. Raskutti, and R. Willett, “Graph-based regularization for regression problems with highly-correlated designs,” in *2018 IEEE Global Conference on Signal and Information Processing (GlobalSIP)*, pp. 740–742, 2018.
- [6] A. Stevens, R. Willett, A. Mamalakis, E. Foufoula-Georgiou, J. T. Randerson, P. Smyth, S. J. Wright, and A. Tejedor, “Graph-guided regularization for improved seasonal forecasting,” in *the 9th International Workshop on Climate Informatics (CI2019)*, (Paris, France), Oct 2019.
- [7] Y. Li, B. Mark, G. Raskutti, R. Willett, H. Song, and D. Neiman, “Graph-based regularization for regression problems with alignment and highly correlated designs,” *SIAM Journal on Mathematics of Data Science*, vol. 2, no. 2, pp. 480–504, 2020.
- [8] A. Stevens, R. Willett, A. Mamalakis, E. Foufoula-Georgiou, A. Tejedor, J. T. Randerson, P. Smyth, and S. Wright, “Graph-guided regularized regression of Pacific Ocean climate variables to increase predictive skill of southwestern US winter precipitation,” *Journal of Climate*, vol. 34, no. 2, pp. 737–754, 2021.
- [9] X. Chen, S. Kim, Q. Lin, J. G. Carbonell, and E. P. Xing, “Graph-structured multi-task regression and an efficient optimization method for general fused Lasso,” *arXiv preprint arXiv:1005.3579*, 2010.
- [10] D. Gabay and B. Mercier, “A dual algorithm for the solution of nonlinear variational problems via finite element approximation,” *Computers & Mathematics with Applications*, vol. 2, no. 1, pp. 17–40, 1976.
- [11] R. Glowinski and A. Marroco, “Sur l’approximation, par éléments finis d’ordre un, et la résolution, par pénalisation-dualité d’une classe de problèmes de Dirichlet non linéaires,” *Revue française d’automatique, informatique, recherche opérationnelle. Analyse numérique*, vol. 9, no. R2, pp. 41–76, 1975.
- [12] J. Eckstein and D. P. Bertsekas, “On the Douglas–Rachford splitting method and the proximal point algorithm for maximal monotone operators,” *Mathematical Programming*, vol. 55, no. 1, pp. 293–318, 1992.
- [13] D. Davis and W. Yin, “Convergence rate analysis of several splitting schemes,” in *Splitting Methods in Communication, Imaging, Science, and Engineering*, pp. 115–163, Springer, 2017.

- [14] Y. Cui, X. Li, D. Sun, and K.-C. Toh, “On the convergence properties of a majorized alternating direction method of multipliers for linearly constrained convex optimization problems with coupled objective functions,” *Journal of Optimization Theory and Applications*, vol. 169, no. 3, pp. 1013–1041, 2016.
- [15] G. Zhang, Y. Yuan, and D. Sun, “An efficient HPR algorithm for the Wasserstein barycenter problem with  $O(\text{Dim}(P)/\varepsilon)$  computational complexity,” *arXiv preprint arXiv:2211.14881*, 2022.
- [16] K. Chen, D. Sun, Y. Yuan, G. Zhang, and X. Zhao, “HPR-LP: An implementation of an HPR method for solving linear programming,” *Mathematical Programming Computation*, vol. 17, 2025.
- [17] D. Sun, Y. Yuan, G. Zhang, and X. Zhao, “Accelerating preconditioned ADMM via degenerate proximal point mappings,” *SIAM Journal on Optimization*, vol. 35, no. 2, pp. 1165–1193, 2025.
- [18] K. Chen, D. Sun, Y. Yuan, G. Zhang, and X. Zhao, “HPR-QP: A dual Halpern Peaceman-Rachford method for solving large-scale convex composite quadratic programming,” *arXiv preprint arXiv:2507.02470*, 2025.
- [19] G. Zhang, Z. Gu, Y. Yuan, and D. Sun, “HOT: An efficient Halpern accelerating algorithm for optimal transport problems,” *IEEE Transactions on Pattern Analysis and Machine Intelligence*, 2025.
- [20] J. Frécon, N. Pustelnik, P. Abry, and L. Condat, “On-the-fly approximation of multivariate total variation minimization,” *IEEE Transactions on Signal Processing*, vol. 64, no. 9, pp. 2355–2364, 2016.
- [21] G. Bassett Jr and R. Koenker, “Asymptotic theory of least absolute error regression,” *Journal of the American Statistical Association*, vol. 73, no. 363, pp. 618–622, 1978.
- [22] D. Pollard, “Asymptotics for least absolute deviation regression estimators,” *Econometric Theory*, vol. 7, no. 2, pp. 186–199, 1991.
- [23] K. Knight and W. Fu, “Asymptotics for Lasso-type estimators,” *The Annals of Statistics*, vol. 28, no. 5, pp. 1356–1378, 2000.
- [24] C. J. Geyer, “On the asymptotics of convex stochastic optimization,” Technical Report, Department of Statistics, University of Minnesota, Minneapolis, MN, 1996.
- [25] R. T. Rockafellar, *Convex Analysis*, vol. 28. Princeton University Press, 1997.
- [26] A. K. Gupta and D. K. Nagar, *Matrix Variate Distributions*. Chapman and Hall/CRC, 1999.
- [27] K. H. Greenewald and I. Alfred O. Hero, “Robust Kronecker product PCA for spatio-temporal covariance estimation,” *IEEE Transactions on Signal Processing*, vol. 63, no. 23, pp. 6368–6378, 2015.
- [28] T. Tsiligkaridis and I. Alfred O. Hero, “Covariance estimation in high dimensions via Kronecker product expansions,” *IEEE Transactions on Signal Processing*, 2013.
- [29] J. E. Kay, C. Deser, A. Phillips, A. Mai, C. Hannay, G. Strand, J. M. Arblaster, S. C. Bates, G. Danabasoglu, J. Edwards, M. Holland, P. Kushner, J.-F. Lamarque, D. Lawrence, K. Lindsay, A. Middleton, E. Munoz, R. Neale, K. Oleson, L. Polvani, and M. Vertenstein, “The Community Earth System Model (CESM) large ensemble project: A community

resource for studying climate change in the presence of internal climate variability,” *Bulletin of the American Meteorological Society*, vol. 96, no. 8, pp. 1333 – 1349, 2015.

- [30] M. Lin and Y. Zhang, “DNNLasso: Scalable graph learning for matrix-variate data,” in *International Conference on Artificial Intelligence and Statistics*, pp. 316–324, PMLR, 2024.